DOI: 10.21062/mft.2025.055 © 2025 Manufacturing Technology. All rights reserved. http://www.journalmt.com

# Study on Material Performance Calculation and Rolling Process Simulation of 35W210X Advanced High Strength Silicon Containing Steel

Tie Ye  $(0000-0003-4218-1017)^1$ , Boran Chen  $(0009-0005-2762-1215)^1$ , Zetian Li  $(0009-0003-7738-0523)^1$ , Zhenyu Gao  $(0009-0001-1124-6300)^2$ , Kuibo Liu  $(0009-0000-3894-7353)^1$ , Zheng Ren  $(0009-0001-5884-3516)^1$ 

<sup>1</sup>Intelligent Manufacturing Research Institute, Nan Yang Normal University, Henan Nanyang 473061, China. E-mail: yetie2009@sina.com, 3011280960@qq.com, 1282669260@qq.com, 1169228863@qq.com, 2065666709@qq.com

<sup>2</sup>Technology Centre of Ansteel Co. Ltd.., Liaoning Anshan 114009, China. E-mail: aggzy@163.com

This study used JMatPro software to comprehensively analyze the new low-iron-loss cold-rolled non-oriented high-grade electrical steel 35W210X, calculating phase composition, Gibbs free energy, stress-strain relationships, and yield strength changes. Results showed its ferritic structure and consistent calculated room-temperature yield strength with experiments. To study production cracks, JMatPro data was used in Deform-3D to simulate the five-pass reciprocating cold rolling on a Sendzimir 20-roll mill, successfully replicating the cracks. Aiming at the problems of frequent cracking and low yield rate (<50%), the study found the original single normalizing annealing process inadequate. Thus, an optimized double annealing process was adopted, controlling cracks and raising the yield rate to over 85%. This research offers theoretical and technological support for rolling high-silicon electrical steels like 35W210X.

Keywords: Non-oriented electrical steel, Crack, JMatPro, Deform-3D

#### 1 Introduction

High-grade non-oriented electrical steel is a critical material for energy-efficient motors and electrical appliances, with stringent requirements for low iron loss and high magnetic permeability[1-3]. Among these, the 35W210X steel, characterized by a high-silicon (3.0-3.5 wt%) and high-aluminum (0.8-1.5 wt%) composition, has emerged as a promising candidate for advanced electrical applications [4]. However, its industrial production faces significant challenges, particularly frequent cracking during cold rolling, which results in a yield rate of less than 50% due to the material's inherent "hard and brittle" nature caused by high silicon content [5-7]. Addressing this issue requires a deep understanding of the material's thermomechanical behavior and rolling process optimization.

Numerical simulation has become an indispensable tool for predicting material performance and optimizing industrial processes. In this study, JMatPro software was employed to computationally analyze the phase composition, Gibbs free energy, and stress-strain relationships of 35W210X steel. These calculations aimed to clarify the microstructural origins of its mechanical properties, such as the absence of austenite transformation and the role of second-phase particles (e.g., AlN, MnS) in magnetic and plastic deformation behaviors [6-8]. Subsequence, the data derived

from JMatPro were integrated into Deform-3D software to simulate the five-pass reciprocating cold rolling process on a Sendzimir 20-roll mill. This simulation sought to replicate real-world rolling conditions, including rolling force fluctuations and crack initiation, to validate the accuracy of the computational model and identify critical process parameters leading to defects [9-10].

The study also focuses on the optimization of heat treatment processes. The traditional single normalizing annealing process was found to be insufficient to control cracking, prompting the development of a modified two-step annealing strategy. By introducing an additional annealing step after the third rolling pass, the research aimed to relieve accumulated stress, suppress the growth of brittle second-phase particles, and improve the material's formability.

Aiming at the common problems in the industrial production of high-grade non-oriented electrical steel, this study combines material calculation and process simulation to establish a cross-scale correlation model of 'composition-structure-performance-process', which provides a reusable technical path for the development of rolling process of high-end electrical steel. This work combines material science calculations, process simulation, and industrial validation to establish a "composition-structure-property-process" integrated framework.

The objectives are threefold:

- 1 To reveal the correlation between the phase composition of 35W210X steel and its cold rolling performance;
- ② To develop a reliable simulation model for predicting crack defects in high-silicon electrical steel;
- 3 To provide a technological basis for improving the yield rate of industrial production.

The findings not only address the practical challenges in manufacturing 35W210X steel but also offer

a reference for the research and development of other high-performance electrical materials.

#### 2 Materials and Software

#### 2.1 Materials

The non-oriented electrical steel 35W210X from China Baosteel Group Co., Ltd. The non-oriented electrical steel 35W210X is characterized by stringent electromagnetic property requirements, with its composition designed on the basis of ultra-low-carbon clean steel. The new material, 35W210X, features a high-silicon (3.0-3.5%) and high-aluminum (0.8-1.5%) alloy design as its main components. The specific composition is detailed in Table 1.

**Tab.** 1 Chemical composition of the steels tested (wt %)

С	Si	Mn	P	S	N	Als	Ti
0.0032	3.25	0.120	0.25	0.0016	0.0018	0.85	0.0015

## 2.2 The performance of electrical steel 35W210X calculated by JMatPro software

JMatPro is a physics-based computational software suite that employs CALPHAD methodology and fundamental metallurgical principles to predict essential material properties and behavior for metallic alloys. Its core functions include calculating phase equilibria, thermodynamic properties, phase transformation kinetics (TTT/CCT diagrams), temperature-dependent physical properties (thermal conductivity, expansion), and mechanical properties (yield strength, stress-strain curves, creep) based on alloy composition [10-12]. A key advantage lies in its robust, critically assessed thermodynamic and kinetic databases, enabling reliable predictions without requiring extensive alloy-specific experimental data. This allows for rapid in silico screening of compositions and processes, significantly reducing experimental costs and time during alloy development and process optimization. Furthermore, JMatPro excels at generating microstructure-sensitive material models for seamless integration into FEM/CFD process simulation software (e.g., Deform), providing accurate input data for realistic modeling of industrial processes like casting, heat treatment, and rolling. Ultimately, it serves as a powerful tool for systematically exploring composition-process-microstructure-property relationships and accelerating materials innovation [13-14].

## 2.2.1 Calculation of 35W210X Alloy Phase Diagram

A comprehensive calculation of the thermodynamic equilibrium phases in 35W210X steel, based on its composition, has been conducted. Specifically, the chemical composition data listed in Table 1 was input into the JMatPro software for thermodynamic

simulation calculations, yielding the thermodynamic equilibrium phase diagram of 35W210X steel (see Fig.1 for details). According to Fig.1, 35W210X steel comprises 11 phase regions, with the primary regions being Liquid and Ferrite, and the remaining nine regions consisting of minimal quantities of phases such as Cementite. These include minimal amounts of AlN, MnS, and various carbide and phosphide phase regions, specifically M7C3, M(C,N), M2(C,N), M2P, M3P, and Ti4C2S2.

Further analysis reveals that the liquidus temperature of 35W210X steel reaches 1411.82°C. As the temperature gradually decreases, ferrite begins to precipitate. When the temperature drops to room temperature, the liquid phase completely transforms into solid ferrite, with no solid-state phase transformation occurring during this process. The absence of Austenite phase transformation is a notable characteristic of non-oriented electrical steel. Based on the calculation data from JMatPro software, it is known that AlN in 35W210X steel begins to dissolve at 1050°C and completely disappears at 1420°C. MnS starts to dissolve at 620°C and its compound disappears at 1110°C. Ti4C2S2 stably exists within the temperature range of 620-940°C. Cementite has a stable existence range of 280-610°C. M7C3 is stable between 110-280°C. M(C, N) is stable within the range of 20-620°C. M2(C, N) has a stable existence range of 20-90°C. M2P is stable between 20-410°C, while M3P is stable within the range of 410-720°C. Ferrite, on the other hand, stably exists within the temperature range of 20-1470°C. These phases, which exist in minimal quantities at room temperature, serve as second-phase particles in electrical steel and have a significant impact on its magnetic properties [12-14].

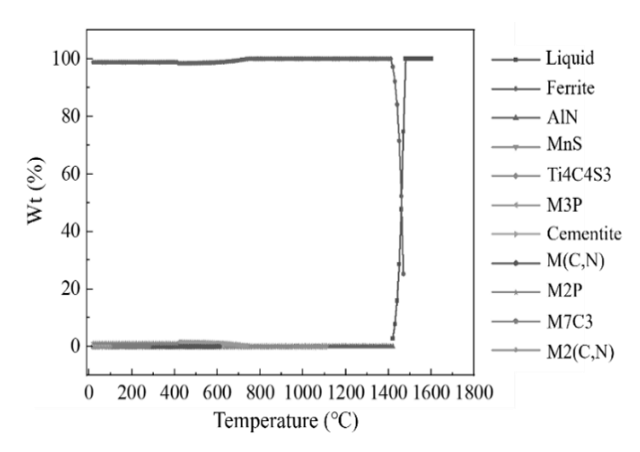


Fig. 1 Phase diagram calculation of 35W210X alloy

#### 2.2.2 Gibbs free energy of 35W210X steel

Figure 2 illustrates the Gibbs free energy of each element in 35W210X steel, calculated using JMatPro software. Observations reveal that the Gibbs free energy of the Fe element remains nearly constant across the entire temperature range, consistently staying at zero, indicating that Fe is the most stable element in this system. As temperature gradually increases, the Gibbs free energy of the N element demonstrates a rising trend, suggesting an enhancement in its stability. Similarly, the Gibbs free energy of both C and Mn elements rises with increasing temperature.

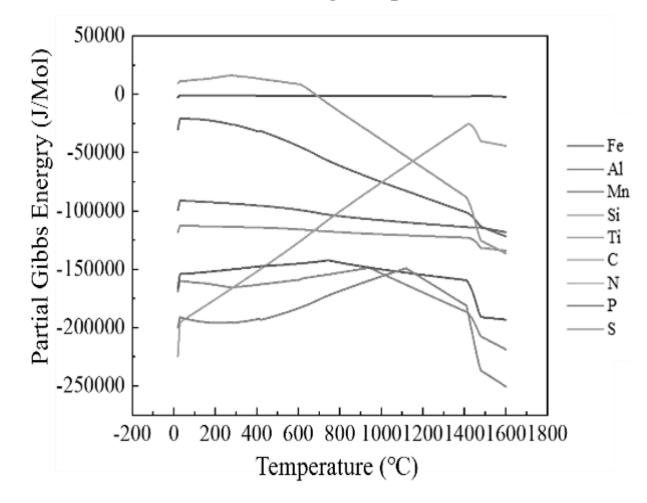


Fig. 2 Gibbs free energy of each element in 35W210X steel

In the actual production process, continuous annealing leads to the precipitation of small amounts of AlN and MnS. The growth of these precipitates significantly affects the magnetic properties of non-oriented electrical steel [15-18]. Therefore, strict control of annealing process parameters is essential during production to ensure the material's magnetic properties meet expected standards. Additionally, the Gibbs free energy curve of the Ti element exhibits a peak at 920 °C, potentially linked to the formation of Ti4C2S2 second-phase particles from titanium, carbon, and sulfur. Notably, these second-phase particles composed of Ti, C, and S also exist in actual 35W210X steel.

#### 2.2.3 Actual measured stress-strain curve

The hot-rolled coil of 35W210X non-oriented electrical steel has a finished thickness set at 2.35mm. The material undergoes heat treatment on a horizontal continuous normalizing production line with a process temperature of 920 °C. Subsequently, samples were taken from the normalized strip steel and subjected to tensile testing on a 30-ton electronic tensile testing machine. The stress-strain curve obtained from the experiment is shown in Figure 3. It is worth noting that 35W210X non-oriented electrical steel did not exhibit a significant yield phenomenon during the tensile process. When the strain  $\varepsilon$  reaches 0.2%, its yield strength is measured to be 390MPa.

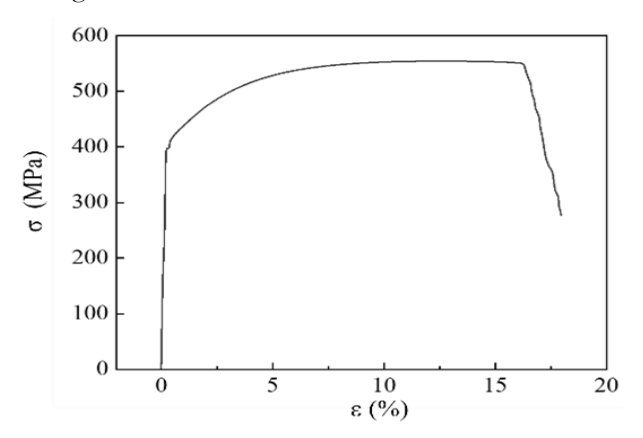


Fig. 3 Stress strain curve of experimental strip steel after normalizing

#### 2.2.4 Calculation of True Stress and True Strain

The true stress is the ratio of the instantaneous load to the instantaneous cross-sectional area, and the true strain is the plastic deformation in the integral form. Compared with the engineering stress-strain change, the true stress and the true strain truly reflect the mechanical behavior of the material under large deformation, see Formula (1)[12]:

$$\sigma_{true} = \frac{F}{A}, \varepsilon_{true} = \int_{L_0}^{L} \frac{dL}{L} = \ln\left(\frac{L}{L_0}\right)$$
 (1)

Where:

F...Load [N],

A...Instantaneous cross-sectional area [m<sup>2</sup>],

 $L_0$ ...Initial lengths [m],

L...Instantaneous lengths [m].

Figure 4 displays the true stress-strain curve obtained through calculations using JMatPro software. Upon comparing Figure 3 with Figure 4, it becomes evident that at room temperature (25°C), the nominal yield value determined by JMatPro aligns with the actual measured value. Nevertheless, in Figure 4, a notable disparity is observed between the engineering strain and the true strain post the yield point. This divergence arises from the comprehensive consideration of the test sample's cross-sectional area changes during plastic deformation in the calculation process.

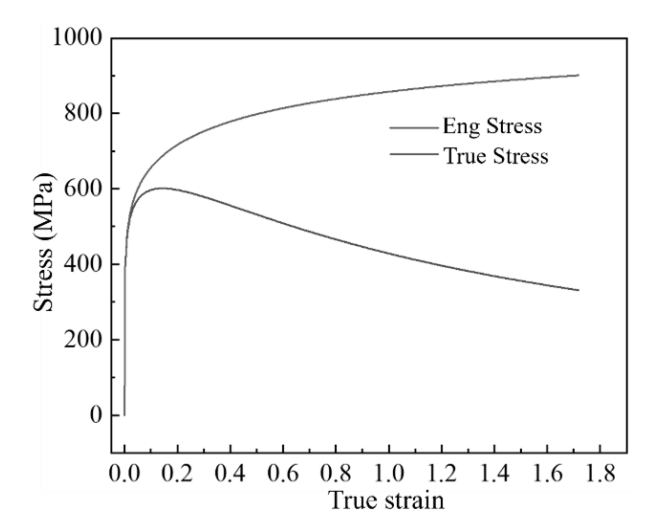


Fig. 4 The true stress-strain curve calculated by JMatPro

JMatPro software employs the DDG (dislocation slip) mechanism at low temperatures and the DDC (dislocation climb) mechanism at high temperatures for calculating material strength. The low-temperature DDG mechanism comprehensively considers the effects of temperature, stress state, and strain rate. Its theory suggests that under low temperature conditions, dislocation movement will be hindered, leading to a pile-up phenomenon, which results in the inability to slip; only when the shear stress increases to a certain extent, can dislocations move and proliferate again. The calculation of intergranular strengthening under this mechanism is carried out using the Hall-Petch formula [19], see Formula (2):

$$\sigma_y = \sigma_0 + k_{den} \lambda^{-0.5} \tag{2}$$

Where:

 $\sigma_y$ ...Yield strength of the material [MPa],

 $\sigma_0$ ...Material-specific constant [MPa],

k...Grain boundary strengthening coefficient,

 $\lambda$ ...Average grain size [µm].

The high-temperature DDC mechanism suggests that in high-temperature environments, dislocations can overcome short-range obstacles and undergo dislocation climb by utilizing the thermal activation energy and vacancy diffusion effect provided by the external environment, thereby causing deformation. The calculation of yield stress adopts the formula (3)[21]:

$$\sigma_{\rm y}({\rm T}) = \alpha + \beta \exp(\frac{-Q}{RT})$$
 (3)

Where:

 $\sigma_v(T)$ ...Yield Strength at Temperature T [MPa],

α...Friction stress or lattice resistance [MPa],

 $\beta$ ...Strengthening coefficient [MPa],

Q...Activation energy for dislocation motion [k]/mol],

R...Universal gas constant, R=8.314 J·mol<sup>-1</sup>·K<sup>-1</sup>,

T...Absolute temperature [K].

Figure 5 shows the stress curve of yield strength as a function of temperature under strain rates of

10-51/s. At room temperature of 25°C, when the strain ε reaches 0.2%, the yield strength of the material is 390.78MPa.

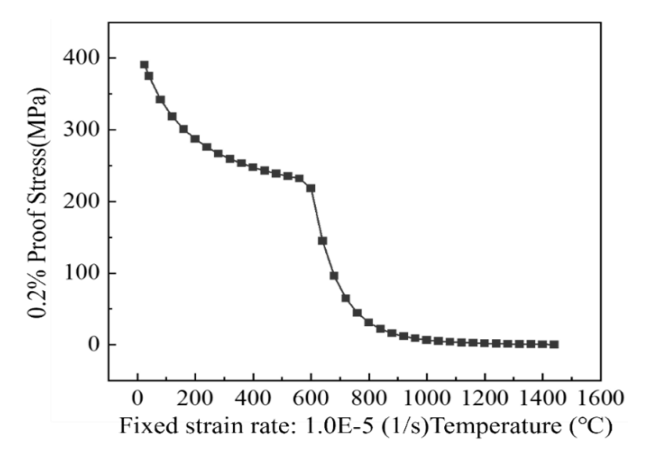


**Fig. 5** Stress curve of yield strength with temperature variation at strain rates of 10-51/s

Figure 6 displays the true stress-true strain curves at various strain rates. These curves reveal the differences in mechanical properties of 35W210X electrical steel material under different loading rates. During the elastic stage, when the strain rate is lower, the curve exhibits relatively smooth characteristics, with a stable elastic modulus. However, at higher strain rates, the elastic modulus increases slightly, reflecting the elastic response characteristics of the material under rapid loading conditions. In the yield stage, as the strain rate increases, both the yield strength and the height of the yield platform show an upward trend. This indicates that under high-speed deformation conditions, a larger external force is required to initiate plastic deformation, demonstrating the material's resistance to high-speed deformation. During the hardening stage, especially at high strain rates, the material becomes more resistant to further plastic deformation during rapid deformation. The rheological stress of the alloy increases at high strain rates, resulting in an increased deformation resistance.

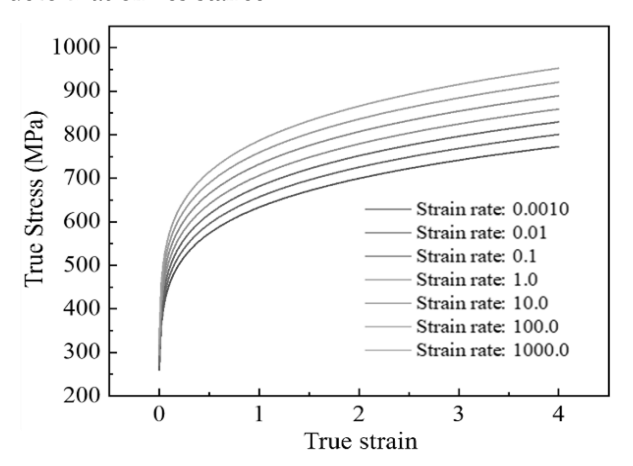


Fig. 6 True strain and true stress curves at different strain rates

## 3 35W210X Electrical Steel Deform-3D Simulation and Rolling

### 3.1 35W210X Electrical Steel Deform-3D Simulation

The cold rolling process of 35W210X electrical steel on a Sendzimir mill was accurately simulated using Deform-3D software. In this simulation, the rolls (work rolls) were set as rigid bodies with a diameter of 60 mm (the actual diameter of the work rolls in a Sendzimir mill), while the blank was set as a plastic body to better align with actual rolling conditions. Since 35W210X non-oriented electrical steel material was not included in the Deform-3D material library, relevant data was calculated using JMatPro software and successfully imported into the simulation environment. The simulation parameter settings for 35W210X electrical steel in Deform-3D are detailed in Table 2.

In the calculation of the rolling process, the Coulomb friction model was adopted, and the friction coefficient was set to 0.07 to ensure the accuracy of the simulation. Additionally, the steel plate used in the simulation had dimensions of  $1000~\text{mm} \times 500~\text{mm} \times 2.35~\text{mm}$ , and a reciprocal rolling method was employed, with a total of five passes to comprehensively simulate the actual rolling process.

The following thermal parameters and conditions were set for the study: the initial temperature of the steel plate was set to 130°C, while the ambient temperature was taken as 20°C, and the roll temperature was set to 25°C. On the free surface of the blank, there were three types of boundary conditions: heat conduction, heat convection, and heat radiation. Specifically, the heat conduction coefficient was set to 1 N/(s·mm·°C), the heat convection coefficient was taken as 0.02 N/(s·mm·°C), and the heat radiation coefficient was set to 0.7. These parameter settings ensured the accuracy and reproducibility of the study.

**Tab. 2** Rolling simulation parameters by Deform-3D

No.	Simulation parameter	Value	
1	Workpiece material	35W210X	
2	Workpiece specimen height (mm)	2.35	
3	Cylinder specimen length (mm)	600	
4	Cylinder specimen diameter (mm)	60	
5	Forging workpiece temperature (°C)	130	
6	Upper and lower die temperature (°C)	25	
7	Conventional coefficient (N/ (s.mm. °C))	0.02	
8	Heat transfer coefficient (N/ (s.mm. °C))	1	
9	Number of deformation steps	1593	
10	Forging environment temperature (°C)	25	
11	Number of elements	50415	
12	Number of nodes	17038	
13	Coefficient of friction (shear-type)	0.07	

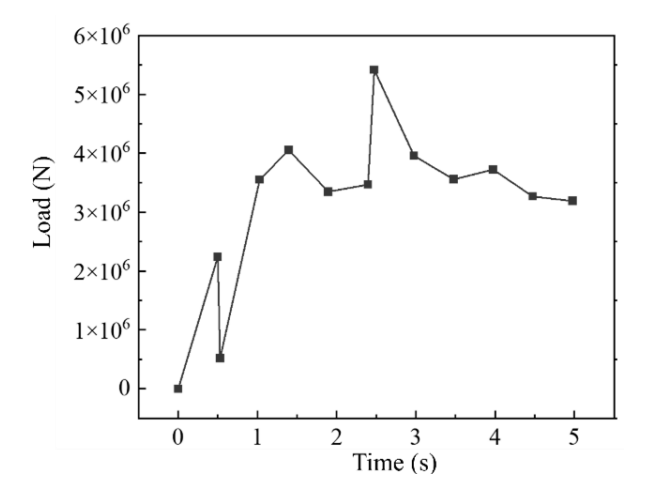


**Fig.** 7 Rolling force at the first pass of  $\triangle h=0.6mm$ 

Figure 7 illustrates the variation of rolling force during the simulation of the first pass in cold rolling. In the simulation setup, the front tension was set to 9 KN, and the back tension was set to 3 KN. According to Figure 7, after 1 second, the fluctuation of the rolling force became relatively stable, indicating that the steel strip entered a relatively stable rolling state after being bitten into the rolls. However, at 2.5 seconds, a relatively large fluctuation in rolling force was observed. This aligns with the rolling force fluctuation monitored during actual production. The speed throughout the rolling process was precisely controlled at  $2\pi$  rad/s, with a reduction amount of 0.6 mm and an average rolling force reaching  $3.5 \times 10^6$  N.

Figure 8 displays the equivalent stress distribution at the contact area between the roll and the steel plate during the simulation of the first pass in cold rolling, specifically at step 7. For ease of observation, the upper die (i.e., the upper roll) has been hidden. Upon observation, it can be found that the equivalent stress at the contact area is not continuously distributed but exhibits a characteristic of being distributed along the

contact line between the steel plate and the roll in a dotted manner. Notably, the locations where these equivalent stresses exist all reach the maximum value in that region, with the red E-marked location representing a stress value as high as 1020 MPa. This phenomenon indicates that these locations are approaching the limit of the flow stress.

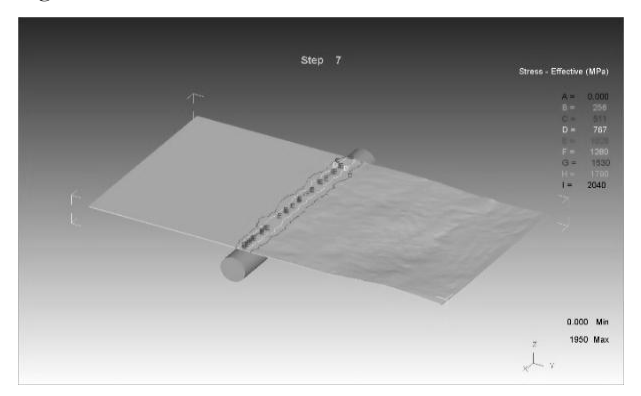


Fig. 8 Stress-Effective at the first pass of  $\triangle h=0.6mm$ 

Figure 9 presents the variation in rolling force during the simulation of the second pass in cold rolling. In the actual simulation process, the front tension was set to 9 KN, while the back tension was set to 8 KN. Due to the adoption of a reversible rolling process, reverse rolling was initiated before the steel strip had completely separated from the rolls. Therefore, in the early stage of rolling, the fluctuation of rolling force was relatively stable, indicating that the steel strip quickly entered a relatively stable rolling state after being bitten into the rolls. However, at the 3-second mark, a significant fluctuation in rolling force occurred, similar to that in the first pass. After the completion of the second pass rolling, the steel strip was allowed to separate from the rolls, and thus at the 11-second mark, the rolling force was displayed as 0. The reduction amount for this pass was 0.4 mm, with an average rolling force reaching 4×106 N.

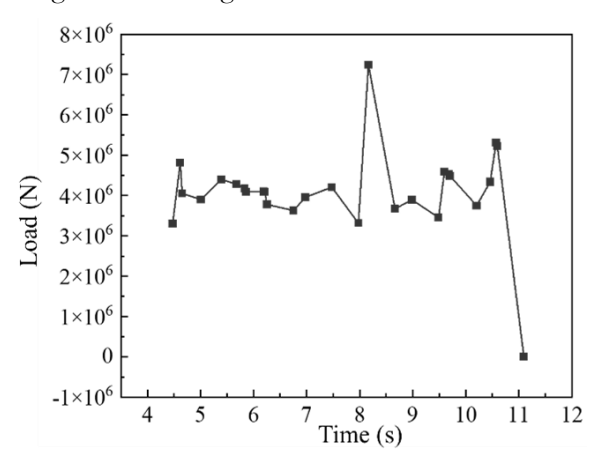
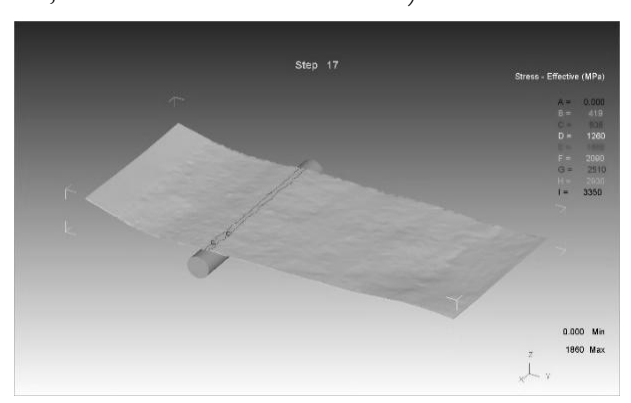


Fig. 9 Rolling force at the second pass of  $\triangle h=0.4mm$ 

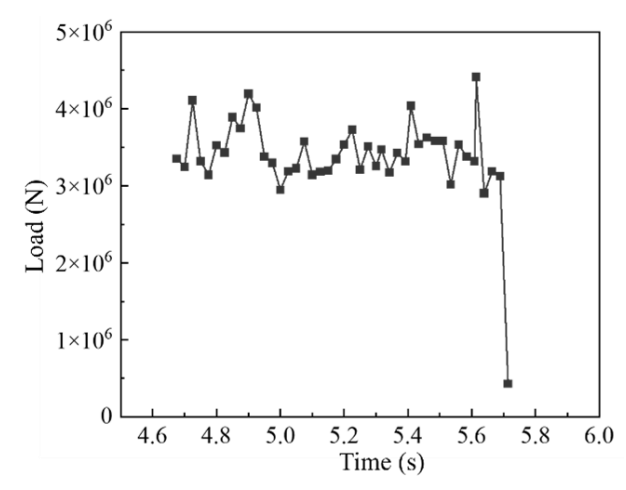
Figure 10 displays the equivalent stress distribution at the contact area between the roll and the steel plate

during the simulation of the second pass in cold rolling, specifically at step 17. Upon observation, it can be found that the equivalent stress at the contact area exhibits a continuous distribution and is mainly concentrated near the positions on both sides of the contact line between the steel plate and the roll. Within the region where equivalent stress exists, there is a location with higher stress (marked with a red C in the figure, with a stress value of 930 MPa).



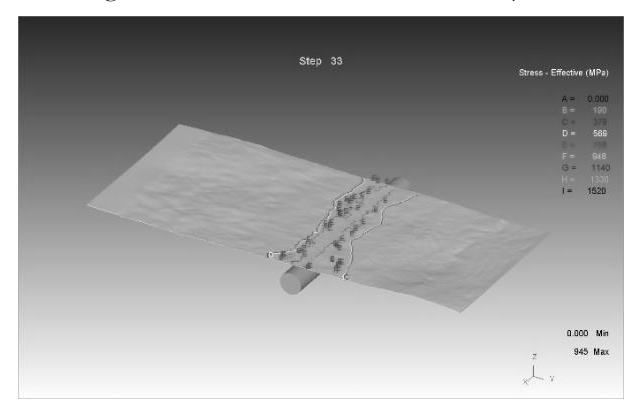
**Fig. 10** Stress-Effective at the second pass of  $\triangle h=0.4mm$ 

Figure 11 demonstrates the variation in rolling force during the simulation of the third pass in cold rolling. In the actual simulation process, the front tension was set to 9 KN, while the back tension was set to 8 KN. After adjusting the steel strip to enter the rolls, the simulation was officially initiated. Throughout the rolling process, the fluctuation of rolling force remained relatively stable, indicating that the steel strip had entered a stable rolling state after undergoing rolling in the first two passes. Notably, due to work hardening that occurred during the first two passes, the rolling force exhibited more stable behavior. Ultimately, the average rolling force for this pass reached 3.5×10<sup>6</sup> N.



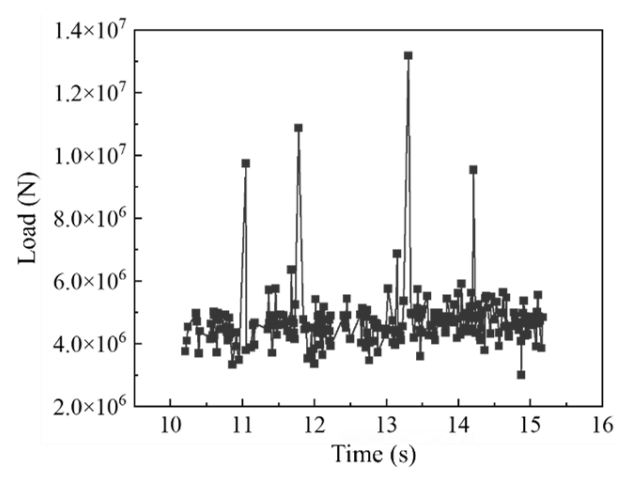
**Fig. 11** Rolling force at the third pass of  $\triangle h=0.4mm$ 

Figure 12 presents the equivalent stress distribution at the contact area between the roll and the steel plate during the simulation of the third pass in cold rolling, specifically at step 33. The observation results reveal that the equivalent stress at the contact area exhibits discontinuous and uneven distribution characteristics. This is primarily attributed to the accumulation of deformation from the first two passes, leading to more severe deformation of the steel strip during this pass. Within the contact region, the equivalent stress reached a maximum value (marked with a red E in the figure, with a stress value of 758 MPa).



**Fig. 12** Stress-Effective at the second pass of  $\triangle h=0.6mm$ 

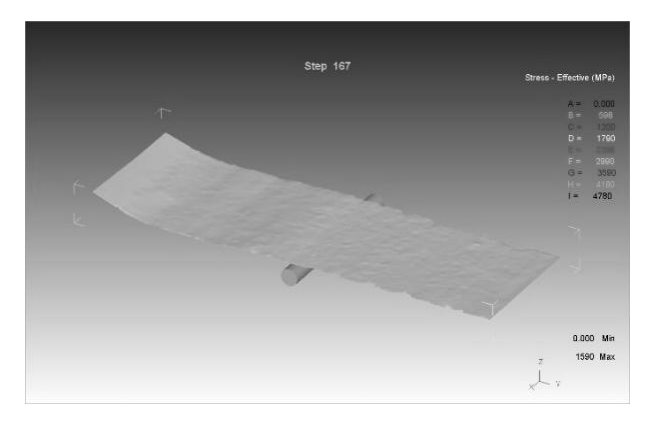
Figure 13 presents the variation in rolling force during the simulation of the fourth pass in cold rolling. In this simulation experiment, the front tension was set to 10 KN, and the back tension was set to 8 KN. As shown in Figure 13, there were four significant fluctuations in the rolling force during the rolling process. This phenomenon indicates that as the deformation accumulates, the deformation resistance of the steel strip gradually increases, leading to violent fluctuations in the rolling force. Despite this, the entire rolling process of the fourth pass remained relatively stable. The reduction amount for this pass was 0.3 mm, and the calculated average rolling force for this pass was approximately 4×106 N.



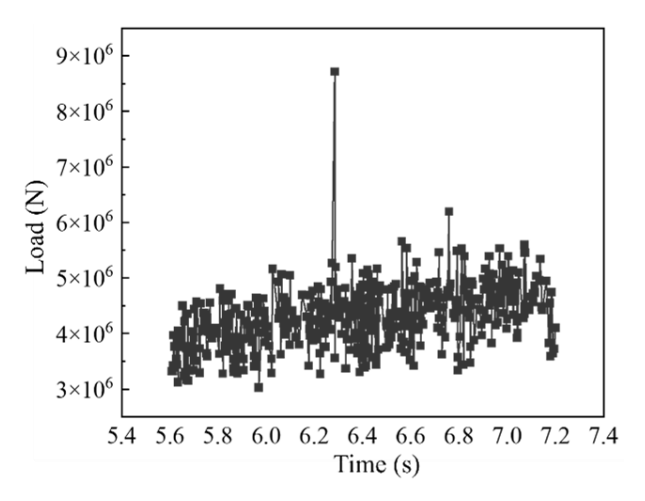
**Fig. 13** Rolling force at the forth pass of  $\triangle h=0.4mm$ 

Figure 14 displays the equivalent stress distribution at the contact area between the roll and the steel plate during the simulation of the fourth pass in cold rolling,

with a set reduction amount of 0.3 mm for this pass. Specifically, at step 167, it can be observed that the equivalent stress at the contact area is relatively low, mainly concentrated in the green region B with a stress value of 560 MPa.



**Fig. 14** Stress-Effective at the forth pass of  $\triangle h=0.3$ mm



**Fig. 15** Rolling force at the fifth pass of  $\triangle h=0.3mm$ 

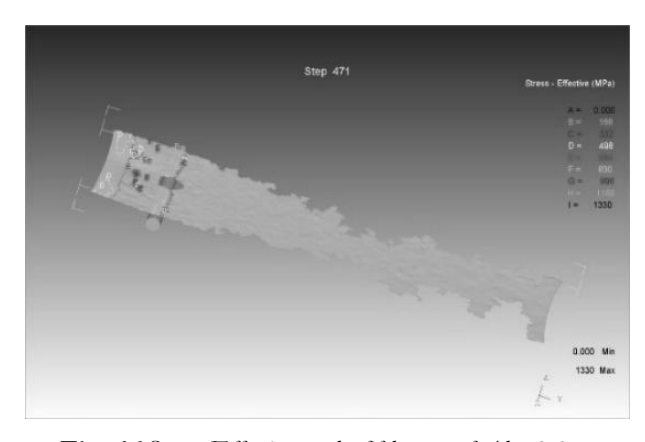


**Fig. 16** Stress-Effective at the fifth pass of  $\triangle h=0.3mm$ 

Figure 15 demonstrates the variation in rolling force during the simulation of the fifth pass in cold rolling. In this simulation experiment, the front tension was set to 7.5 KN, and the back tension was set to 8 KN. As shown in Figure 15, a significant fluctuation in rolling force occurred during the rolling process. The reduction amount for this pass was also

0.3 mm, with no notable increase in deformation or deformation resistance. Under these conditions, the fluctuation in rolling force remained relatively stable. Overall, the entire rolling process of the fifth pass maintained a relatively stable rolling state. Calculations revealed that the average rolling force for this pass was approximately  $4\times10^6~\rm N$ .

Figure 16 illustrates the equivalent stress distribution at the contact area between the roll and the steel plate during the simulation of the fifth pass in cold rolling, specifically at step 471. The observations revealed severe edge cracks and mid-section openings in the steel strip. The equivalent stress at the crack locations, indicated by the red region E in the figure, reached 664 MPa. Compared to other regions, the equivalent stress value at these locations was higher and exhibited a concentrated distribution with a higher density. Despite the fact that the reduction amount for this pass was only 0.3 mm, resulting in moderate deformation of the steel strip, the

cumulative reduction amount had already reached 2 mm, and the thickness of the steel strip at this point was only 0.35 mm, approaching the limit of rollable thickness. Therefore, multiple cracks formed during the rolling process, which gradually expanded during subsequent rolling passes, ultimately leading to the openings observed.

#### 3.2 Actual rolling of 35W210X electrical steel

The actual production process of 35W210X electrical steel cold-rolled coil is completed through five cycles of reciprocating rolling on the Sendzimir rolling mill. The raw materials used are hot-rolled coils that have undergone normalization and acid washing treatment. The weight of the incoming material is 20 tons, with a width of 1250mm and a thickness of 2.35mm. Before the cold rolling process begins, the steel plate will undergo preheating treatment. The specific rolling process parameter settings can be found in Table 3.

**Tab. 3** Chemical composition of the steels tested (wt %)

Main rolling parameters	Control of each rolling pass						
Rolling pass	1	2	3	4	5		
Compression amount (mm) 0.6	0.6	0.4	0.4	0.3	0.3		
Front tension (KN) 9.0	9.0	9.0	9.2	10	7.5		
Rear tension (KN) 3.0	3.0	8.0	8.0	8.0	8.0		
Temperature (°C) 130	130	100	80	80	80		
Speed (m/min) 100	100	150	150	150	150		
Rolling force (KN) 4.0	4.0	4.0	3.5	4.0	4.0		

In the actual cold rolling production process, it was observed that 35W210X steel exhibits a "hard and brittle" characteristic due to its high silicon content. This characteristic leads to edge cracking and mid cracking phenomena during the rolling process [19-21], as shown in Figures 17 and 18. The circled part in Figure 17 shows the side of the steel coil, with edge cracks hidden in the gaps. The part circled in Figure 18 is the intermediate crack and fissure generated by rolling. It is worth noting that this phenomenon is consistent with the simulation results of Deform-3D, further verifying the accuracy of the simulation model.

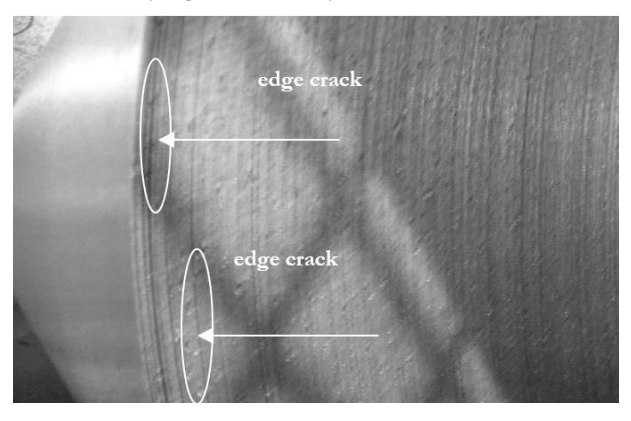


Fig. 17 Cracks at the edge of the strip steel

In response to the frequent cracks in 35W210X non-oriented electrical steel during actual production, which led to a yield rate of less than 50%, measures were taken to improve the heat treatment process. The original once normalizing annealing process was adjusted to a twice process, adding a second annealing after the third rolling pass. Simultaneously, the rolling reduction was optimized, reducing the third pass to 0.3mm and increasing the fourth pass to 0.4mm. These improvements yielded significant results.

Based on production data from 50 batches (25 preimprovement and 25 post-improvement), crack detection was performed using an online visual inspection system (±0.1 mm precision) to measure crack length and density in each coil. Coils with crack lengths exceeding 5 mm/m were deemed unqualified. The weight qualification rate was calculated as the ratio of qualified product weight to total input raw material weight, excluding steel coils scrapped due to cracks. A two-sample t-test ( $\alpha$ =0.05) confirmed a statistically significant difference (p<0.01) between yield rates: the average pre-improvement yield was 48.7% (standard deviation ±3.2%), rising to 86.2% (standard deviation ±2.5%) post-improvement. Combined with qualified weight ratio analysis, the modified annealing processes increased the yield rate from 48.7% to 86.2%

(95% confidence). This process improvement effectively controlled crack formation in 35W210X non-oriented electrical steel during rolling, elevating the yield rate to over 85%. The optimization enhanced production efficiency, increased material utilization, significantly reduced costs, and improved product quality.

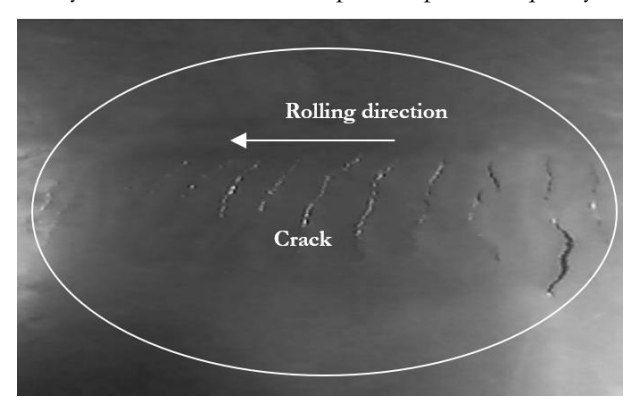


Fig. 18 Cracks at the middle of the strip steel

#### 4 Conclusions

- 1) The newly developed 35W210X non-oriented electrical steel has 11 phases, with ferrite as the main matrix (over 95% at room temperature) and trace secondary phases (e.g., AlN, MnS). It shows no austenite transformation, consistent with non-oriented electrical steels' solid-state non-phase transformation behavior. JMatPro-calculated room-temperature yield strength (390.78 MPa) matches the experimental value (390 MPa). Yield strength is defined at 0.2% strain due to the absence of a distinct yield plateau.
- 2) Deform-3D simulations of five-pass Sendzimir cold rolling replicated rolling force fluctuations and crack formation. High equivalent stress (up to 1020 MPa) at the roll-strip interface in early passes initiated edge/mid cracks, which propagated with deformation. Results matched production observations, confirming high silicon content causes "hard-brittle" behavior and localized cracking. The JMatPro-Deform-3D approach proved reliable for process optimization.
- 3) Based on Deform-3D simulation, it is revealed that the single annealing process has high crack sensitivity (crack incidence > 50 %) due to residual work hardening, while the two annealing processes (650 °C × 2h annealing after the third pass) can refine the

average grain size from  $8~\mu$  m to  $5~\mu$  m, and the density of the second phase particles is reduced by 32 %. Combined with the optimization of rolling reduction (0.3mm in the third pass  $\rightarrow$  0.4mm in the fourth pass), the yield is finally increased to more than 85 %, which meets the requirements of industrial production.

#### Acknowledgement

We would like to thank the Key Research and Development Projects of Henan Province (No. 242102230064), Project of Education Department of Henan Province (No. 212300410377).

#### References

- [1] FAN, L.F., QIN, M.M., YUE, E.B. (2021). Technological Challenges of New Energy Vehicle to Non-oriented Silicon Steel. *Materials Review*, pp. 15183-15188. DOI:10.11896/cldb.20050259.
- [2] YU, L. LUO, H.W. (2020). Effect of Partial Recrystallization Annealing on Magnetic Properties and Mechanical Properties of Non-Oriented Silicon Steel. *Acta Metallurgica Sinica*, pp. 10. DOI: 10.1007/s11837-022-05444-4
- [3] ZHANG, W.R. (2017). Effect of Annealing Temperature and Cr Element on Microstructure and Properties of Electrical Steel, Hot Working Technology, pp. 222-224. DOI 10.1088/1757-899X/231/1/012131
- [4] JIAO, H.T. (2017). High-permeability and thingauge non-oriented electrical steel through twin-roll strip casting, *Materials & Design*, pp. 23-33. DOI: 10.1016/j.matdes.2017.09.051
- [5] MOHAMED, S. (2020). Fatigue Strength and Fracture Mechanisms in the Very - High - Cycle-Fatigue Regime of Automotive Steels. *Steel Research International*, pp. 12-17. DOI: 10.1002/srin.202000060
- [6] WANG, Y.D. (2025). Study on Transverse Surface Cracks in the Continuous Casting Slab of a Microalloyed Steel. Steel Research International, pp. 13-16+38. DOI: 10.1002/srin.202400988
- [7] GAO, Y.J. (2019). Study on microstructure evolution and properties of Fe-3.1% Si steel for new energy vehicles by adjusting normalizing temperature. *Journal of Physics: Conference Series*, 012137. DOI: 10.1088/1742-6596/2951/1/012137

- [8] ZHAO, T.L. (2017). Corrosion fatigue crack initiation and initial propagation mechanism of E690 steel in simulated seawater. *Materials Science and Engineering: A*, pp. 181-192. DOI: 10.1016/j.msea.2017.09.078
- [9] ALBIN, G.B. (2023). Cyclic deformation behavior of non-oriented electrical steel sheets. *Materials Science and Engineering: A*, pp. 145684. DOI: 10.1016/j.msea.2023.145684
- [10] XU, Y.T (2017). Phase Composition and Cracking Behavior of Co-8.8Al-9.8W-0.2B Alloy in TIG Welding Layer Based on JMatPro Software. Rare Metal Materials and Engineering, pp. 2459-2464. DOI:10.3321/j.issn:1001-053X.2008.12.009
- [11] XU, Y.T., SHA, Q.Z. (2016). Thermodynamic simulation calculation of precipitated phases in Co-8.8Al-9.8W alloy with different B contents based on JMatPro software. Rare Metal Materials and Engineering, pp. 2332-2336. DOI:10.3969/j.issn.1001-3784.2012.04.001
- [12] HUA, Y.X., LI, J.G., ZHANG, C. (2015). High Temperature Mechanical Properties of 50W470 Non-oriented Electrical Steel. *Hot Working Tech-nology*, pp. 64-66. DOI: 10.14158/j.cnki.1001-3814. 2015.18. 018.
- [13] ISAKOV, D.V., KOROTKOV, V.A. (2021). The Influence of Carbonitration on the Magnetic Properties of Electrical Steel. Russian Electrical Engineering, pp. 56-58. DOI: 10.3103/s1068371221010041
- [14] ZU, G.Q., XU, Y.Q., LUO, L. (2022). Effect of rolling temperature on the recrystallization behavior of 4.5 wt.% Si non-oriented electrical steel. *Journal of Materials Research and Technology*, pp. 365-373. DOI: 10.1016/j.jmrt.2022.01.027
- [15] FANG, F. (20222). Microstructure evolution and strengthening mechanism in thin-gauge

- non-oriented silicon steel with high strength. *Journal of Magnetism and Magnetic Materials*, pp. 169791. DOI: 10.1016/j.jmmm.2022.169791
- [16] WEN, Q.Y. (2024). Effect of high magnetic field annealing on microstructure, texture, and properties of high-strength non-oriented silicon steels. *Journal of Materials Research and Technology*, pp. 2252-2262. DOI: 10.1016/j.jmrt.2024.09.223
- [17] JIAO, H.T. (2022). Role of Hot Rolling in Microstructure and Texture Development of Strip Cast Non-Oriented Electrical Steel. *Metals*, pp. 12. DOI: 10.3390/met12020354
- [18] HE, Y.L. (2017). Skew rolling and its effect on the deformation textures of non-oriented electrical steels. *Journal of Materials Processing Technol*ogy, pp. 182-195. DOI: 10.1016/j.jmatprotec.2016.11.033
- [19] YE, T., ZHOU, C., GAO, Z.Y. (2014). Comprised of hot rolled material with high temperature coiling and normalization material for the production of high grade nonoriented silicon steel. *Journal of Functional Materials Journal of Functional Materials*, pp. 110-114+120. DOI:10.3969/j.issn.1001-9731.2014.03.025
- [20] ZHANG, Z.G., LIU, Y.D., W, F. (2010). Effect of annealing time on recrystallization texture and magnetic property of non-oriented silicon steel under asynchronous rolling. *Transactions of Materials and Heat Treatment*, pp. 69-72. https://xuebao.neu.edu.cn/natural/EN/Y2007/V28/I8/1131
- [21] LU, J.D., WU, S.J., YU, C.X. (2021). Effect of secondary annealing temperature on microstructure and magnetic properties of nonoriented silicon steel. *Heat Treatment of Metals*, pp. 67-71. DOI: 10.13251/j.issn.0254-6051.2021.03.013